Renewable Energy 253 (2025) 123564

Contents lists available at ScienceDirect

Renewable Energy

journal homepage: www.elsevier.com/locate/renene

Spatially varying seasonal modulation to tidal stream energy potential due to mixed tidal regimes in the Aleutian Islands, AK

Preston Spicer [a,*], Zhaoqing Yang [a,b], Taiping Wang [a], Mithun Deb [a]

[a] Coastal Sciences Division, Pacific Northwest National Laboratory, Seattle, WA, USA
[b] Department of Civil and Environmental Engineering, University of Washington, Seattle, WA, USA

ARTICLE INFO

Keywords:
Tidal stream energy
Mixed tides
Alaska

ABSTRACT

We provide an assessment of the tidal stream energy resource of the Aleutian Islands, Alaska via a validated barotropic tidal numerical model of the region. Eight island passes are identified as energy "hotspots". The annual mean kinetic energy fluxes, *KEF*, calculated at each pass vary from 1000 to 11,000 MW, while the annual available energy, *AAE*, varies from 5 to 42 MWh m^{-2}. Notable seasonal modulation to monthly power density averages and ranges are noted at some passes and not others. Seasonal adjustment is linked to the semi-annual solar declination cycle which enhances (dampens) diurnal (D_1) tidal amplitudes in summer/winter (spring/fall) as well as the time-varying phase lag between D_1 and semidiurnal (D_2) fortnightly tidal cycles. Annual variability in monthly mean power density scales with the tidal current form factor, F_u, with the largest seasonal change occurring for $F_u > 1$ (D_1 dominated tide). The spread in power density over a month is on average smaller for passes with mixed tides ($F_u = 1$) than those with D_1 or D_2 dominance, as changes to fortnightly phase lag become influential to net power density ranges when tides are mixed. This study outlines overlooked, but relevant, long-term modulation to tidal streams in regions with mixed tides.

1. Introduction

Globally, climate change and population growth are spurring countries to diversify and augment energy resources. Renewable energies have been heavily pursued in recent years due to their less impactful carbon footprints and long-term sustainability. Tidal stream energy is one such source and utilizes predictable ebbing and flooding currents driven by astronomical tides to spin underwater turbines, creating energy. Multiple regions in the United States have strong tidal currents and have been identified as tidal energy "hotspots", though the state of Alaska holds the vast majority of the theoretical resource (e.g., Ref. [1,2]). Estimates indicate all of Alaska's energy needs could be powered by tides [2]. This is particularly important there, as the state struggles with supplying affordable energy to its many remote communities which are often not connected to state/national electricity grids and largely depend on expensive fuel oil that is inefficiently transported great distances [3]. Energy prices per capita in Alaska are the second highest in the nation, partly due to the state's sizable petroleum dependence coupled with a harsh winter climate [4]. As such, multiple locations in the state are being considered for tidal stream turbine deployments, for both grid-scale and remote, non-grid power production (e.g., Ref. [5–7]).

An understudied, but tidally energetic region in Alaska is the Aleutian Islands. The region is comprised of thousands of islands and extends over 1300 km west from the Alaska Peninsula to the Kamchatka Peninsula of Russia, forming a border between the Bering Sea and greater Pacific Ocean. Large tidal amplitudes in the North Pacific drive relatively fast tidal currents through the many relatively narrow, shallow passes between islands (e.g., Ref. [8]; Hunt Jr & Stabeno, 2005; [9]). Communities on the islands are often small (<1000 inhabitants), geographically isolated, powered by diesel-fueled generators, and so particularly prone to astronomical energy costs [10]. Co-location of the remote communities with significant tidal currents illustrates great potential for localized, non-grid scale tidal energy production. Preliminary analyses of theoretical tidal-diesel systems in southern Alaska suggest a modest 56 kW influx of tidal energy (3 turbines here) could offset ~$56,000 in diesel fuel cost and 244,000 lb. in CO_2 emissions, annually [11]: a significant economic and environmental boon for a community. A single other tidal energy feasibility study has been conducted at False Pass in the Aleutians (e.g., Ref. [12]), even though multiple locations in the

This article is part of a special issue entitled: Ocean Energy Resource 2024 published in Renewable Energy.

* Corresponding author.
E-mail address: preston.spicer@pnnl.gov (P. Spicer).

https://doi.org/10.1016/j.renene.2025.123564
Received 26 August 2024; Received in revised form 21 April 2025; Accepted 24 May 2025
Available online 25 May 2025
0960-1481/

archipelago are ranked within the top 10 tidal stream resources of the entire country [1]. A comprehensive evaluation of the spatial and temporally varying resource potential over the entire region has yet to be performed.

The Aleutian archipelago features dramatic variability in tidal range and frequency. Tidal ranges vary from microtidal (<2 m) around some western islands to macrotidal (>4 m) near the Alaskan mainland [13]. The tidal form factor, $F = \frac{A_{K1}+A_{o1}}{A_{M2}+A_{S2}}$, where A represents the amplitudes of the K_1, O_1, M_2, and S_2 astronomical constituents (subscripts), illustrates further variability. In the western Aleutians, the tide is diurnal ($F > 3$) or mixed, mainly diurnal ($F = 1.5 - 3$). Moving east towards the mainland, the tides become a mixed, mainly semidiurnal regime ($F = 0.25 - 1.5$) (e.g., Ref. [14]). Diurnal tides ($K_1 + O_1$) are subject to spring-neap (13.66 day) amplitude modulation based on lunar declination, while semidiurnal tides ($M_2 + S_2$) follow a similar, but slightly offset, 14.76-day schedule, according to sun and moon alignment. Diurnal tides are also seasonally modulated: solar declination creates larger tidal ranges around the winter and summer solstice, and smaller in spring and autumn. Mixed tides are adjusted at both timescales, creating complicated, varying patterns of tidal elevations and currents over months and years. Even so, there are no studies to date which have investigated how tidal regime modulates tidal stream power estimates, if at all. It appears likely that temporally varying amplitudes and phase differences between the daily and twice daily tides would correspondingly be impactful to temporal variability in tidal stream power, but this has yet to be shown or quantified.

The primary goal of this paper it to provide a first assessment of the tidal energy resource of the Aleutian Islands, Alaska and determine the role of tidal regime (e.g., diurnal, semidiurnal, mixed) in modulating that resource. The objectives of the study are: (1) quantify mean and time varying tidal energy metrics at several locations in the Aleutian Islands, (2) classify each location by tidal regime, (3) and identify the impact of tidal regime on energy potential statistics at each location. Section 2 provides more information on tides around the Aleutians. Section 3 presents the numerical model used to conduct this study, observations utilized for model validation, and model skill compared to observations. Tidal energy characterization metrics, formulations, and results used to evaluate the objectives are presented in Section 4. In Section 5 we discuss the broader implications of our findings, future work, and limitations. Lastly, the conclusions of this study are given in Section 6.

2. Aleutian Island Tides

The significant tidal stream energy potential of the Aleutian Islands is largely a result of the unique geography of the region. The Aleutian

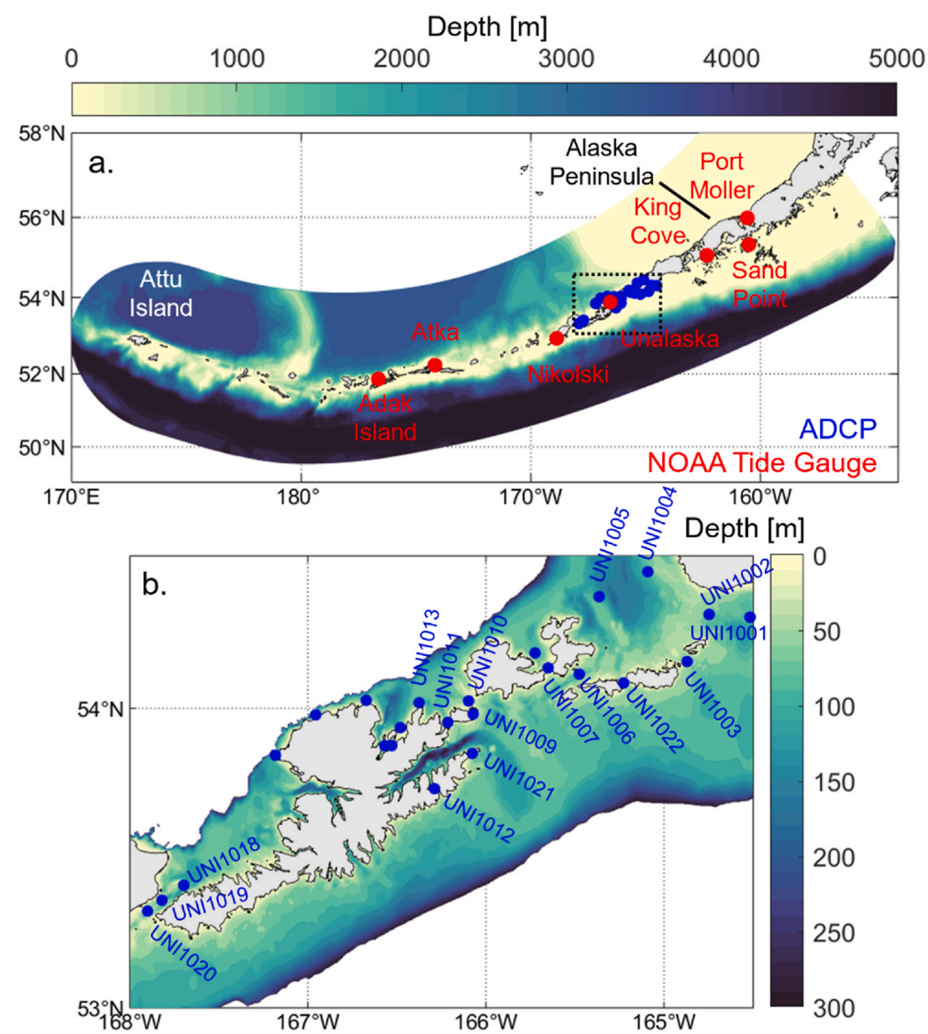

Fig. 1. (a) Full model domain with bathymetry (colored contours) and locations of ADCP observations (blue) and NOAA tide gauges (red). (b) Zoom-in on ADCP sampling region. NOAA tide gauge names are labeled in (a) while ADCP names are given in (b). Only ADCP locations with maximum current speeds greater than 0.1 m/s are labeled. Note: color bars depict different depth ranges in each subplot. Depth contours maximize at 300 m in (b). Place name references are also given in black or white lettering in (a). (For interpretation of the references to color in this figure legend, the reader is referred to the Web version of this article.)

Islands form an arc spanning an impressive 4 degrees of latitude and 25 degrees of longitude, separating the North Pacific Ocean from the Bering Sea (Fig. 1). The eastern end of the arc connects to the Alaskan mainland and sits between two major coastal basins: Bristol Bay to the north and the Gulf of Alaska to the south. Depths straddling the island chain are hundreds to thousands of meters deep, but rapidly shallow approaching the islands. Where land does not exist along the arc, there are relatively narrow (10s of kilometers) and shallow (10s–100s of meters) passes which control the majority of exchange between the North Pacific and Bering Sea (Hunt Jr & Stabeno, 2005; [9,15]). The passes act as constrictions which greatly enhance tide induced currents moving through them, while simultaneously dissipating tidal energy from significant current shear and eddy shedding both vertically and horizontally [8].

Edge amplification and reflection in Bristol Bay and the Gulf of Alaska, coupled with tidal energy dissipation through the island passes, creates the spatial variability in tides outlined in Section 1 [13]. Over most of the region, the K_1 and M_2 frequencies dominate the diurnal and semidiurnal tides, respectively, and are representative of spatial variability in those constituents (i.e., K_1 for O_1, P_1, Q_1 and M_2 for S_2, K_2, N_2). A_{K1} varies from ~0.7 m to ~0.35 m east to west along the Aleutians, with amplification near mainland Alaska attributed to edge reflection in Bristol Bay, where A_{K1} maximizes near 1 m A_{M2} is similarly maximized along the Gulf of Alaska coast, south of the Aleutians, and exceeds 1 m. Over the Aleutians proper, A_{M2} decays from ~0.8 m near King Cove to a minimum of 0.2 m West of Adak Island (see Fig. 1). Both K_1 and M_2 have degenerative amphidromic points at locations inside (for M_2) and northwest (for K_1) of Bristol Bay, creating intense spatial variability in tidal amplitude just north of the eastern Aleutians.

Both semidiurnal and diurnal tides propagate south to north through the Aleutians [16–18], but the M_2 is affected the most by energy dissipation in the island passes. This is largely a result of M_2 having relatively stronger tidal currents which enhance frictional losses [13,19]. Dissipation of M_2 creates a notable reduction in amplitude (up to 20 cm) and phase (up to 180°) from south to north across the Aleutian archipelago, particularly near the mainland. Gradients for K_1 are more modest (maximum 10 cm decrease in amplitude and 45° in phase). Collectively, the complex geography and bathymetry of the region allow strong but spatially dynamic tidal currents through a number of passes in the Aleutians. It is at some of these locations we find the greatest potential for tidal energy extraction.

3. Methods

3.1. Tidal Hydrodynamic Model

To comprehensively evaluate the tidal energy potential of the Aleutians, a 3D, barotropic tidal hydrodynamic numerical model was utilized. We use the Finite Volume Community Ocean Model (FVCOM), a general-purpose ocean model with an unstructured grid that is particularly amiable in modeling coastal regions with complex geography [20]. FVCOM solves the 3D Reynold's averaged Navier-Stokes equations of continuity and momentum with Bousinessq assumptions in hydrostatic mode. More detail on the theory and formulation applied to FVCOM are provided in Chen et al. [20]. Though the model is run in 3D mode, a 2D model would be sufficient to perform the analysis and describe the dynamics used in this paper. We ran the model in 3D to broaden the utility of the model output for future work related to tidal energy: particularly tidal turbine siting and array design.

The grid for the numerical model follows the Aleutian Island arc and starts on the Alaska Peninsula near Kodiak Island and ends just west of Attu Island at the 170° E meridian (Fig. 1). The domain holds a roughly 5° north-south width along the extent of the arc. The unstructured grid was created using the Surface-water Modeling System (SMS), and variable cell sizes were determined by topography (higher resolution around islands and in passes) and area transitions between adjacent cells (area transition ratio of 0.7 required). Cell resolution varies from ~2.5 km at the open boundaries to ~150 m within the island passes, meeting the criteria for a Stage 1 tidal energy feasibility study recommended by the International Electrotechnical Commission for tidal energy resource assessments [21] and also providing sufficient resolution to capture fine scale coastal features and straits important to Aleutian Island tidal transport. The IEC threshold has been frequently utilized in recent tidal stream energy modeling work as a first-guess minimum resolution (e.g., Ref. [22–25]). In total, there are ~400,000 nodes and ~800,000 triangular elements (cells) in the domain. Vertical resolution varies over the domain and is set by 10 uniform, terrain-following sigma layers. Bathymetry data was acquired from the National Oceanic and Atmospheric Administration (NOAA) 100-m smoothed sheet bathymetry compilation of the Aleutian Islands [26], which comprises most of the model grid. Regions not included in the 100-m data include deep regions south of the shelf break in the North Pacific/Gulf of Alaska and the western tip of the Aleutians. In these regions we applied NOAA's ETOPO1 1 Arc-Minute Global Relief Model bathymetry. The combined bathymetry sets were interpolated onto the model grid.

Tides were the only forcing mechanism applied to the model, as the major aim of this work is to provide an assessment of tidal energy potential. No major rivers are present within the domain which would be consequential to coastal dynamics or currents at tidal time scales. In reality, vertical and horizontal density gradients in both temperature and salinity occur due to the convergence of multiple coastal currents in the region (e.g., Hunt Jr & Stabeno, 2005) which allow baroclinic flows [27], but they are considered of second order importance to barotropic transport at tidal time scales [9], particularly within the passes. As such, these model simulations are run in barotropic mode. Wind and waves are known to be quite energetic in the region [28], but we omit wind/wave forcing from these model runs to focus on tide-only currents. Future work is planned to elucidate the influence of wave-current interaction on tidal power potential around Alaska. Tides were applied to the model open boundary via free surface elevation time series obtained from the Oregon State University (OSU) TPXO global ocean tide database [29]. In total, 13 tidal constituents were used: M_2, S_2, K_2, N_2, K_1, O_1, P_1, Q_1, M_4, MS_4, MN_4, M_m, and M_f.

We initialized the model with zero free surface elevation and velocity. After three days of tidal forcing, the model reached dynamic equilibrium. A single, yearlong simulation was run from June 1, 2010, to June 1, 2011. The period was chosen as it overlaps with acoustic Dopplar current profiler (ADCP) observations taken in the summer of 2010 used for model validation, while a year-long record allows a wide-spectrum of possible tidal variability (apart from nodal tides) to be considered in analysis. Model results were output every hour over the full year at each grid node and cell. Bottom friction was specified via a bottom drag coefficient, $C_d = 0.005$, and roughness height, $Z_0 = 0.005$ m, which define the logarithmic bottom layer following the quadratic law. The chosen C_d and Z_0 values were chosen following a preliminary sensitivity analysis testing different combinations of each variable and are considered sufficient for this study.

As this is a first step resource characterization, no tidal turbines are simulated. Turbines may be parametrized in FVCOM as momentum sink terms, such as in Deng et al. [30]; Spicer et al. [23]; Spicer et al. [24]; and Yang et al. [31]. Future work will test the impact of various turbine array configurations in the Aleutian Islands.

3.2. Observational Data

Sea surface elevations at 7 NOAA tide gauges and current velocity profiles at 25 ADCP stations were used to validate the model (Fig. 1). The permanent tide gauges are located at (from west to east, Fig. 1): Adak Island (NOAA ID = 9461380), Atka (9461710), Nikolski (9462450), Unalaska (9462620), King Cove (9459881), Sand Point (9459450), and Port Moller (9463502). The temporary ADCP stations were also deployed by NOAA over various date ranges generally between June 10, 2010, and September 11, 2010 (Table 1). Although 25

Table 1
ADCP sampling locations, deployment durations, positions, and sampling depths. Only ADCP locations with maximum current speeds greater than 0.05 m/s are described.

Station ID	Location	Start Date	End Date	Latitude	Longitude	Depth Range [m]
UNI001	Unimak Pass, East Approach	November 6, 2010	7/24/2010	54.2998	−164.5169	7.8–71.8
UNI002	Unimak Pass	November 6, 2010	November 9, 2010	54.3086	−164.7468	8.9–64.9
UNI003	Ugamak Strait	7/24/2010	November 9, 2010	54.1545	−165.8709	8.3–38.3
UNI004	Unimak Pass, North Approach	October 6, 2010	7/24/2010	54.4483	−165.0912	10.7–65.7
UNI005	Unimak Pass, West Approach	October 6, 2010	7/25/2010	54.3669	−165.3643	8.7–74.7
UNI006	Avatanak Strait	November 6, 2010	7/23/2010	54.1127	−165.4757	12.3–75.3
UNI007	Akun Strait	November 6, 2010	7/23/2010	54.1337	−165.6511	3.3–23.3
UNI009	Baby Pass	October 6, 2010	7/23/2010	53.9812	−166.0717	6.6–40.6
UNI010	Akutan Pass	December 6, 2010	November 9, 2010	54.0245	−166.0975	9.1–63.2
UNI011	Unalga Pass	October 6, 2010	7/23/2010	53.9537	−166.2147	7.8–47.8
UNI012	Udagak Strait	7/28/2010	October 9, 2010	53.7341	−166.2890	5.8–33.8
UNI013	Priest Rock	October 6, 2010	7/22/2010	54.0185	−166.3756	4.3–42.3
UNI018	Paso Point	7/27/2010	September 9, 2010	53.4124	−167.6974	11.0–81.0
UNI019	Umnak Pass	7/27/2010	October 9, 2010	53.3623	−167.8198	11.6–77.6
UNI020	Konets Head	7/27/2010	October 9, 2010	53.3259	−167.9006	9.7–53.6
UNI021	Sedanka Pass	7/28/2010	October 9, 2010	53.8512	−166.0763	7.9–59.9
UNI022	Derbin Strait	December 6, 2010	7/23/2010	54.0839	−165.2270	10.2–67.2

ADCP stations were deployed, 17 were used for validation purposes (those labeled in Fig. 1 and listed in Table 1) as 8 locations outside of the main passes measured maximum currents less than 0.1 m/s: too small for effective tidal stream energy conversion with enhanced error in model-data comparison from nontidal current biases. All ADCPs were bottom-mounted, upward facing, sampled at 6 min intervals, and had a 1.76 m vertical blanking distance between the instrument and first sampling bin. All instruments were Teledyne Workhorse ADCPs with frequencies of 300 kHz (16 stations) or 600 kHz (1). Vertical bin sizes were: 5.0 m (2 stations), 4.0 m (1), 3.0 m (5), 2.0 m (7), or 1.0 m (2). Instruments were mounted either 5.5 m (14 stations) or 20 m (3) off the bottom. The various instrument configurations allowed anywhere from 20 to 80 m of the water column to be sampled (Table 1).

3.3. Estimating the Tidal Energy Resource

The tidal current power density, P, was used to identify regions of high energy potential in our domain:

$$P = \frac{1}{2}\rho u_p^3 \tag{1}$$

where ρ is the density of seawater (1025 kg m^{-3}), and u_p is the current velocity rotated to the principal axis direction. Equation (1) can be calculated with current velocities varying or averaged in time and space, making it a useful metric to quantify the unaltered (i.e., no turbines present) power potential of currents. To identify hotspots in our domain, we calculated Equation (1) at every horizontal grid cell in the model domain using time (annual: denoted with an overbar and subscript, a) and depth averaged currents. Passes with elevated depth averaged $\overline{P_a}$ relative to the remainder of the domain were then classified as tidal energy hotspots and further characterized by section (pass) averaged quantities. Namely, we estimated the annual mean kinetic energy flux, KEF, and annual available energy, AAE, through each section similar to Yang et al. [25] and Ahn et al. [32]:

$$KEF = \sum_{j=1}^{N_{cell}} \overline{P_a} A_{cell} \tag{2}$$

$$AAE = T_{year} \frac{KEF}{\sum_{j=1}^{N_{cell}} A_{cell}} \tag{3}$$

where N_{cell} is the number of grid cells comprising a section, A_{cell} is the area of each cell face (in the vertical plane), and T_{year} is the number of hours in a typical year (8766 h). Equation (2) describes the annual average bulk energy flux through each section from tidal currents, some portion of which could be convertible to tidal energy. Equation (3) is a metric for annual energy production per unit area, so is not skewed by section area and indicates which sections have the most concentrated energy potential.

4. Results

4.1. Model Validation

4.1.1. Water Levels

Modeled water levels are shown relative to tide-only predictions at each NOAA gauge location in the domain for a 15-day period (Fig. 2). Comparisons are favorable, though discrepancies are noted at Port Moller in the daily higher-high and higher-low waters which we diagnose below. Spring-neap variability is well-captured, as well as semidiurnal, diurnal, and mixed tidal regimes. Importantly, Fig. 2 illustrates the transition in tidal regime from Port Moller (mixed, semidiurnal) to Adak Island (diurnal).

Four statistical error metrics were calculated to quantify model skill in reproducing tidal water levels at each NOAA gauge. The parameters were calculated using the entire year-long model time series. The root-mean-square-error, $RMSE$, is taken as:

$$RMSE = \sqrt{\frac{\sum_{i=1}^{N}(M_i - O_i)^2}{N}} \tag{4}$$

where N is the total number of observed and modeled data points, O_i is the measured (observed) value, and M_i is the predicated (modeled) value. The scatter index, SI, is $RMSE$ normalized by the average magnitude of measurements, $\overline{|M|}$:

$$SI = \frac{RMSE}{\overline{|M|}} \tag{5}$$

The bias quantifies the averaged difference between observations and predictions:

$$Bias = \frac{\sum_{i=1}^{N}(M_i - O_i)}{N} \tag{6}$$

And the linear correlation coefficient, R, quantifies the strength of the linear relationship between observations and modeled results:

$$R = \frac{\sum_{i=1}^{N}(M_i - \overline{M})(O_i - \overline{O})}{\sqrt{\left(\sum_{i=1}^{N}(O_i - \overline{O})^2\right)\left(\sum_{i=1}^{N}(M_i - \overline{M})^2\right)}} \tag{7}$$

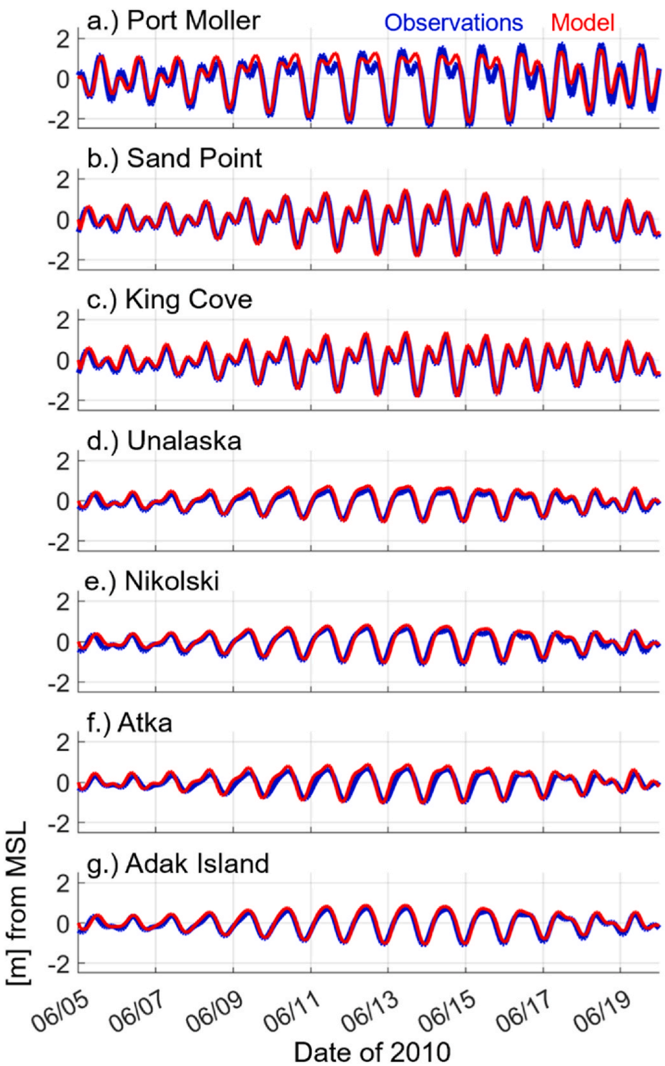

Fig. 2. NOAA tide predictions (blue) and model results (red) over a 15-day period in 2010 (*x*-axis). Comparisons are made at Port Moller (a), Sand Point (b), King Cove (c), Unalaska (d), Nikolski (e), Atka (f), and Adak Island (g) NOAA tide stations. (For interpretation of the references to color in this figure legend, the reader is referred to the Web version of this article.)

At all locations west of Port Moller, *RMSE* is between 0.1 and 0.14 m, indicating error is small relative to tidal ranges of 2 m or larger. At Port Moller, the *RMSE* is elevated to 0.32 m, a result of the imperfect model representation of observed higher-high and higher-low waters (Fig. 2a). Even so, *SI* for Port Moller (0.41) is within the range of the other locations (0.19–0.54), suggesting a decent fit is still achieved. For all gauges, bias is quite small (−0.01 to 0.048), and *R* is greater than 0.93, further indicating model representations are reasonable (Table 2).

We augment the model-data time series statistics with a comparison of amplitudes and phases for the four most significant tidal constituents in the region: M_2, K_1, O_1, and P_1 (Fig. 3). Harmonic analyses were performed on the year-long free surface elevation observations (and corresponding model output) at each NOAA gauge using the UTide MATLAB toolbox [33], from which amplitude and phase were determined. In general, amplitudes and phases match well for most frequencies at most locations. Harmonic analysis reveals the model error at Port Moller is largely a result of the M_2 amplitude being underpredicted by ~20 cm relative to observations (Fig. 3a). The K_1 and O_1 amplitudes are also underpredicted at Port Moller, but to a lesser extent (<10 cm, Fig. 3c–e). Interestingly, the phases for all constituents at all locations are well captured, regardless of amplitude discrepancies. We suspect the model skill is reduced at Port Moller due to the complexity of tides within and near Bristol Bay, the sub-basin on which the port sits. Both the diurnal and semidiurnal tides experience extreme spatial variability in amplitude within the bay due to the presence of degenerate amphidromic points nearby [13]. It is possible the tidal open boundary condition does not resolve spatial variability perfectly, which would create error in tidal propagation and amplitudes nearby. Regardless, we find tidal water levels to be well-resolved over the remainder of the model domain, particularly in the Aleutian Island passes, where the bulk of our analysis occurs.

Table 2
Water level error statistics at the six NOAA stations determined from the full year time series.

Station Full/Short Names	RMSE [m]	SI	Bias [m]	R
Port Moller/POR	0.32	0.41	0.015	0.94
Sand Point/SAN	0.14	0.25	−0.007	0.98
King Cove/KIN	0.10	0.19	−0.010	0.99
Unalaska/UNA	0.12	0.38	0.027	0.97
Nikolski/NIK	0.13	0.39	0.018	0.95
Atka/ATK	0.17	0.54	0.048	0.93
Adak Island/ADA	0.10	0.29	0.030	0.98

4.1.2. Currents

Modeled depth averaged currents were similarly compared to measured currents at each ADCP station. Fig. 4 compares east-west (u) and north-south (v) depth averaged currents at six ADCP locations spanning the sub-section of the model domain where currents were measured (Fig. 1b), while Fig. 5 portrays time series of the principal axis directed depth-averaged velocity at the same locations. Depth averaging covers the vertical sampling range of each ADCP and not necessarily the entire water column. Modeled and observed current speeds and direction match favorably at the six stations and show largely unidirectional flooding and ebbing currents differing in direction by 180°, indicative of tide dominated flow (Fig. 4). Further, good agreement exists in time varying current velocity and phase between the observations and model (Fig. 5). Figs. 4 and 5 also illustrate generally fast currents occur in the island passes but significant variability occurs over relatively small spatial distances. For example, a 1 m/s difference in max current speed exists between UNI1002 (max ~ 2 m/s) and UNI1005 (max ~ 1 m/s), which are both located in Unimak Pass, while max speeds in nearby Unalga Pass (UNI1011) are considerably larger (~4 m/s).

Error statistics (Equations (4)–(7)) were also calculated for depth-averaged currents at all ADCP stations described in Table 1. Currents were rotated to their principal directions prior to applying (1) through (4). Most locations show good agreement between modeled and observed currents with $SI < 0.5$, bias <0.3 m/s, and $R > 0.92$ (Table 3). Locations with poorer comparisons include UNI1004, UNI1013, UNI1018, and UNI1021, where *SI* approaches 1 and *R* ranges from 0.79 to 0.89. These locations are generally outside of the major passes and experience weaker current speeds (<1 m/s). As a result, they are more prone to modulation from non-tidal mechanisms such as wind and surge, which are not included in our tide-only model. Even so, we see that the Aleutian Islands model performs quite well even with omission of other processes. Tides account for a significant portion of the depth-averaged current signal in the region, allowing *R* values to generally remain above 0.9 (Table 3).

4.2. Energetic Passes

Elevated $\overline{P_a}$ was present throughout the Aleutians, but we identified the largest quantities to occur between 164° W and 180° W, in the western (Fig. 6a) and central (Fig. 6b) regions. Here, we see relatively small spatial zones of elevated $\overline{P_a}$ (>1 kW m^{-2}) located in the shallow passes quickly transitioning to broad swaths of $\overline{P_a}$ near 0 kW m^{-2} in

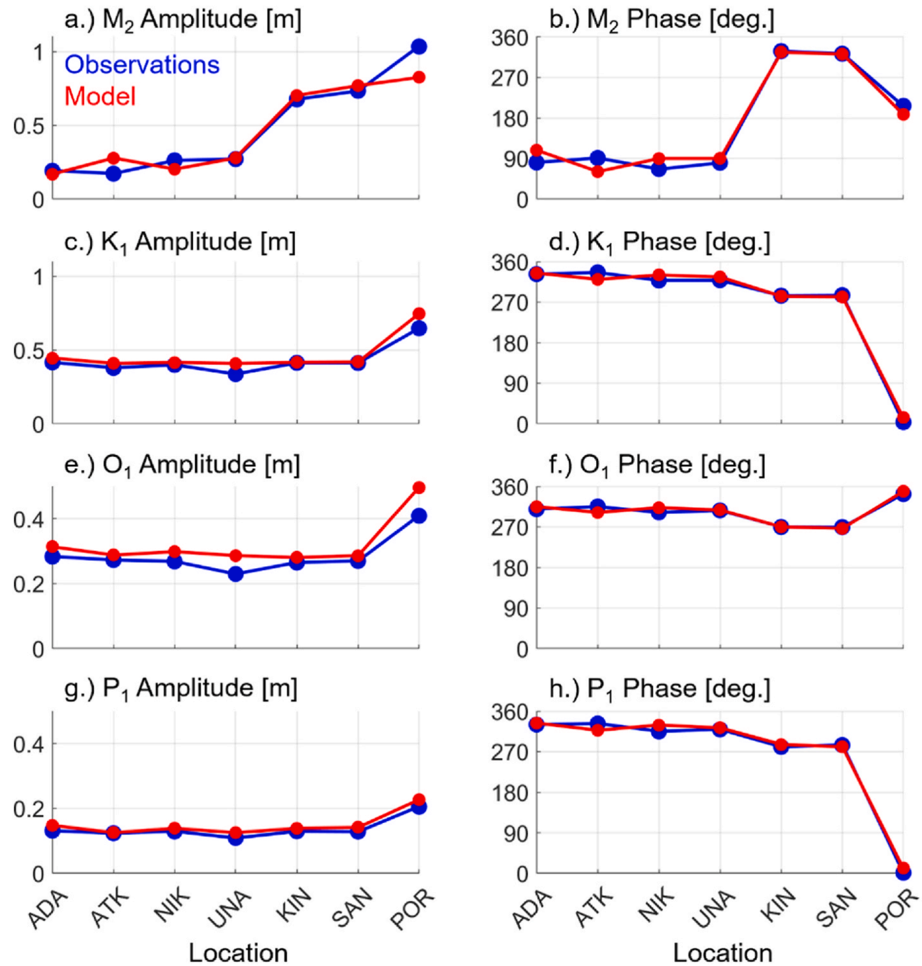

Fig. 3. Tidal sea surface height amplitudes (a, c, e, g) and phases (b, d, f, h) for observations (blue) and model results (red) at the seven NOAA stations (*x*-axes). The four most significant tidal constituents are shown: M_2 (a, b), K_1 (c, d), O_1 (e, f), and P_1 (g, h). Corresponding full names for the abbreviations on the *x*-axes are shown in Table 2. Usage of year-long time series resulted in 95 % confidence interval error bars too small to visualize. (For interpretation of the references to color in this figure legend, the reader is referred to the Web version of this article.)

deeper waters (Fig. 6): an expected result mirroring the intense spatial variability in currents throughout the archipelago. We located eight island passes with depth averaged $\overline{P_a}$ greater than 1.5 kW m^{-2} and the greatest potential for tidal stream energy (from a raw power perspective).

The eight passes are numbered in Fig. 6 and further described in Table 4. Depths and dimensions for each pass were taken from Zimmermann and Prescott [15]. Sill depths for the selected passes range from 47 m at Atka Pass to 372 m at Tanaga Pass; lengths vary from ~6 km at Fenimore Pass to ~33 km at Tanaga and Samalga Passes; and cross-sectional areas vary from 195,000 m^2 at Akutan Pass to 4,180,000 m^3 at Tanaga Pass (Table 4). We created sections roughly following the cross-channel axis of each pass in FVCOM, through which we calculated *KEF* and *AAE* (Fig. 7). Annual average *KEF* typically lies between 1000 and 2000 MW, although sections 6 (Samalga) and 5 (Sequam) greatly exceed these values at ~7000 MW and ~11,000 MW, respectively (Fig. 7a), due to their relatively large cross-sectional areas (Table 4) coupled with evenly distributed, elevated power densities (Fig. 6b). *AAE* largely varies between 5 and 25 MWh m^{-2} with a maximum of 42 MWh m^{-2} occurring at section 7 (Akutan, Fig. 7b), the location with the smallest cross-sectional area (Table 4) and largest power density (Fig. 6b).

4.3. Tidal Regimes

Thus far, we have accomplished objective 1 of this study by identifying the most energetic tidal streams in the Aleutian Islands and quantifying annual mean energy metrics (power density, kinetic energy flux, and annual available energy) at each pass location. Objectives 2 and 3 require characterizing each pass by tidal regime (2) and quantifying the impact of tidal regime on energy metrics (3).

Here, we use the tidal form factor for free surface amplitudes, $F = \frac{A_{K1}+A_{o1}}{A_{M2}+A_{S2}}$ (described in section 1), and principal axis currents, $F_U = \frac{U_{K1}+U_{o1}}{U_{M2}+U_{S2}}$ (where U is the principal axis current amplitude for each constituent), to identify tidal regimes at each section. A and U for each frequency were determined using harmonic analysis via UTide, where section averaged free surface and current velocities over the full year duration were applied as inputs. Typically, form factors >3 indicate a diurnal tidal regime, <0.25 is semidiurnal, 0.25–1.5 is mixed, mainly semidiurnal, and 1.5–3 is mixed, mainly diurnal. F and F_U show notable variability through the selected sections and sometimes opposing tidal regimes depending on whether current or free surface amplitude is considered (Table 4). Sections 1, 2, 4, 5, and 7 feature diurnal tidal elevations while sections 3 and 6 are mixed, diurnal; and section 8 is mixed, semidiurnal. Conversely, tidal currents indicate sections 2 thru 8 are mixed, semidiurnal and section 1 is mixed, diurnal. In the coming sections, we identify and quantify tidal regime impacts on tidal stream energy metrics and unravel the importance of sea surface versus current-defined

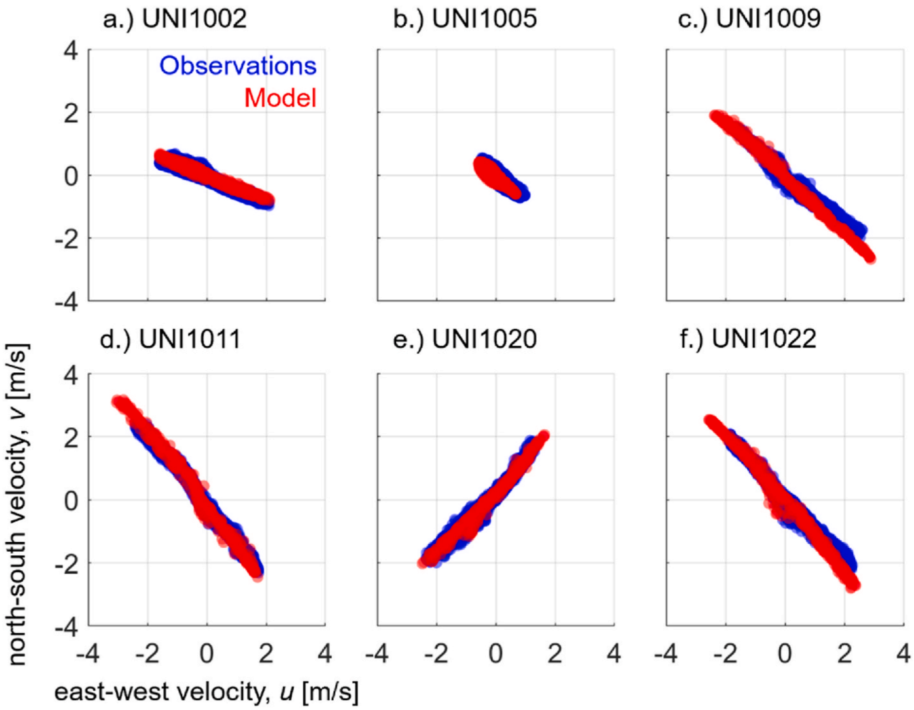

Fig. 4. Scatter point comparisons of 15 days of depth-averaged north-south (*y*-axes) and east-west (*x*-axes) current velocities for observations (blue) and model results (red) at six ADCP stations: UNI1002 (a), UNI1005 (b), UNI1009 (c), UNI1011 (d), UNI1020 (e), and UNI1022 (f). (For interpretation of the references to color in this figure legend, the reader is referred to the Web version of this article.)

tidal regime in characterizing those impacts.

4.4. Spatiotemporal Variability in Tidal Streams

To illustrate the impact of tidal regime on power density, we first decomposed section averaged u_p into diurnal, D_1, and semidiurnal, D_2, components and applied Equation (1) to the D_1, D_2, and combined D_1+D_2 constituents. Amplitudes and phases of the 8 major semidiurnal and diurnal constituents used to force the model (M_2, S_2, K_2, N_2, K_1, O_1, P_1, and Q_1) were determined at each section using UTide, then applied to reconstruct time series of each frequency at each section over the full year. We then summed the diurnal frequency time series for a bulk diurnal tide ($D_1 = K_1 + O_1 + P_1 + Q_1$) and the semidiurnal frequencies for a bulk semidiurnal tide ($D_2 = M_2 + S_2 + K_2 + N_2$). The combined D_1+D_2 tide accounts for 96 %–99 % of the variance of the modeled tidal signal across the sections, suggesting tidal variability is largely explained by the eight D_1 and D_2 constituents (see Appendix A).

In Fig. 8, we show the decomposition at three sections representing (according to *F*) diurnal (section 1, $F = 3.73$, $F_u = 1.84$), mixed, mainly diurnal (section 6, $F = 1.75$, $F_u = 0.96$), and mixed, mainly semidiurnal (section 8, $F = 1.28$, $F_u = 0.55$) regimes. As F and F_u would suggest, diurnal tides decrease in importance moving from section 1 to 6 while semidiurnal tides increase. At all sections, we also see the D_1 and D_2 fortnightly cycles are nearly perfectly out of phase: i.e., spring D_1 occurs during neap D_2 (e.g., Aug. 14). We calculated P for the D_1 and D_2 current velocity components, as well as the combined D_1+D_2, and took running, daily (25 h) means at each section (denoted $\overline{P_d}$) to highlight variability longer than a day for comparison to the long-term annual mean ($\overline{P_a}$). At section 1, $\overline{P_d}$ including all constituents largely trends with $\overline{P_d}$ for D_1-only: two distinct peaks occur where $\overline{P_d} > \overline{P_a}$ which coincide with D_1 spring tides (Fig. 8d–j). Between the D_1 peaks, a trough occurs ($\overline{P_d} < \overline{P_a}$), though it coincides with a D_2 spring tide that prevents the summed tide $\overline{P_d}$ from "bottoming-out" near 0 kW m^{-2}. At section 6, D_1 and D_2 tides seem equally impactful to the combined $\overline{P_d}$. Only one peak occurs where $\overline{P_d} > \overline{P_a}$, falling between the first D_1 and D_2 spring tides (August 8, Fig. 8k). After the $\overline{P_d}$ peak, an extended period occurs where $\overline{P_d} \sim \overline{P_a}$ (August 14 to 26, Fig. 8k), and there is no appreciable deviation from the long-term mean as similar magnitude D_2 then D_1 spring tides occur in succession. Lastly, the combined $\overline{P_d}$ at section 8 follows the D_2 tide closest: one major peak occurs ($\overline{P_d} > \overline{P_a}$) which coincides with the larger D_2 spring tide (August 13, Fig. 8l). $\overline{P_d}$ then falls below $\overline{P_a}$ on either side of the spring tide. Collectively, Fig. 8 portrays a scenario when the differing spring-neap cycle periods for D_1 (13.66 d) and D_2 (14.76 d) tides are out of phase, creating multiple modes of $\overline{P_d}$ variability over a month which appear dependent on tidal regime. Considering the D_1 and D_2 fortnightly cycles become in-phase every ~177 days, and the D_1 tide is known to vary seasonally, we next expand the temporal limits of Fig. 8 to a full year to identify longer modes of variability driven by tidal regime.

Seasonal variability to $\overline{P_d}$ becomes evident, particularly at locations with strong D_1 currents, when a full year is considered (Fig. 9). At all sections the seasonal adjustment to D_1 by solar declination is clear: D_1 amplitudes are largest around December and June 21, and smallest near September and March 21 (Fig. 9d, e, f). Seasonal variability is not present in the D_2 currents, as expected (Fig. 9g, h, i). The result is a noted increase (decrease) to the combined tide $\overline{P_d}$ in the winter/summer (spring/autumn) months with $\overline{P_d} > \overline{P_a}$ ($\overline{P_d} < \overline{P_a}$) at sections 1 and 6 (Fig. 9j and k). Conversely, no notable seasonal change to $\overline{P_d}$ occurs at section 8, where D_1 currents are not important to power density (Fig. 9l), and deviations above/below $\overline{P_a}$ are mainly driven by the D_2 spring/neap cycle. We also see times when the 1.1-day-offset D_1 and D_2 fortnight cycles fall into phase (twice per year), contrary to the pattern observed in Fig. 8. In 2010/2011 the in-phase periods happen to coincide with the seasonal maxima for D_1 (e.g., November to January and May to July) and out-of-phase periods with the D_1 minima (e.g., February to April and August to October, Fig. 9j, k, l).

We have qualitatively identified two mechanisms which likely modulate P_d seasonally. Seasonal adjustment to D_1 tides from solar declination is straightforward and doing as one would expect: increasing the D_1 power density contribution in summer/winter and decreasing it in spring/autumn. The impact of the shifting D_1/D_2 fortnightly cycle

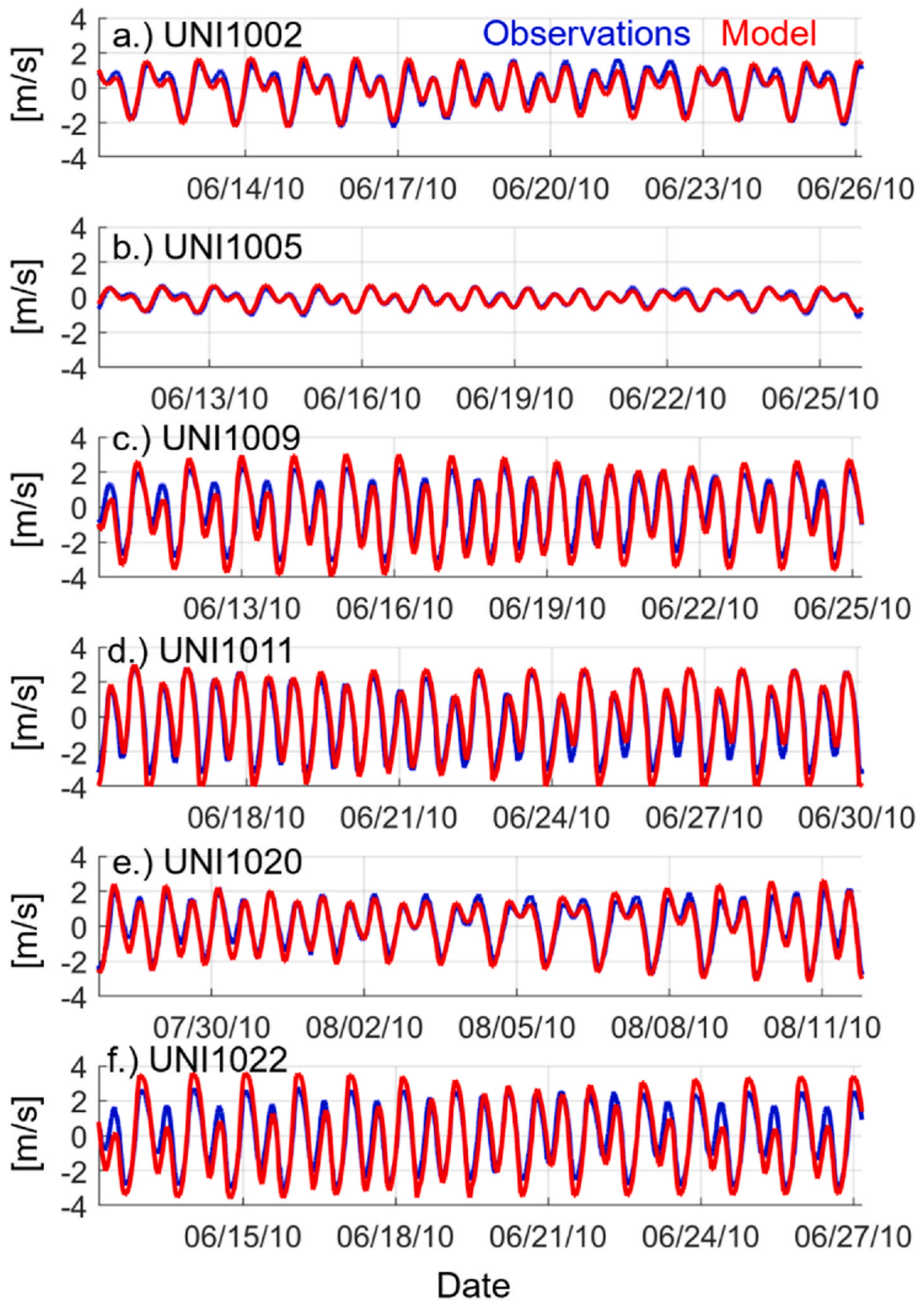

Fig. 5. Time series comparisons of 15 days of depth-averaged principal axis directed current velocities for observations (blue) and model results (red) at six ADCP stations: UNI1002 (a), UNI1005 (b), UNI1009 (c), UNI1011 (d), UNI1020 (e), and UNI1022 (f). (For interpretation of the references to color in this figure legend, the reader is referred to the Web version of this article.)

phase lag is more obscure but appears to impact power density ranges over a fortnight or month (Fig. 8). We next move toward a more quantitative evaluation of seasonal variability in $\overline{P_d}$ to properly scale the importance of each modulation and identify tidal regime thresholds associated with each.

4.5. *Quantifying Tidal Regime Impacts to Power Density Throughout the Aleutian Islands*

To quantify seasonal and bulk annual variation in power density, we took monthly means of P (denoted $\overline{P_m}$) for each month at each section and normalized by that section's $\overline{P_a}$. As such, $\overline{P_m}/\overline{P_a} > 1$ indicates a monthly mean power density larger than the annual average, and $\overline{P_m}/\overline{P_a} < 1$ indicates the opposite. We then quantify bulk change at each section over the year with $\Delta(\overline{P_m}/\overline{P_a})$: i.e., the annual range in monthly normalized mean power density. Similarly, we quantify variation *within* each month as the range in $\overline{P_d}$ (denoted $\Delta\overline{P_d}$) normalized by $\overline{P_m}$. $\Delta\overline{P_d}/\overline{P_m}$ describes the spread in power density over a month relative to the monthly mean, therefore omitting the influence of seasonal changes to mean P. A larger $\Delta\overline{P_d}/\overline{P_m}$ value indicates a relatively larger monthly range in power density. We took an annual mean, $\overline{\Delta\overline{P_d}/\overline{P_m}}$, to identify which sections tend to produce the largest power density ranges, and quantified the temporal connection to the D_1-D_2 fortnightly phase lag, φ, with a Pearson correlation coefficient between $\Delta\overline{P_d}/\overline{P_m}$ and φ, named $\rho_{\Delta\overline{P_d},\varphi}$.

Spatiotemporal variation in $\overline{P_m}/\overline{P_a}$ and $\Delta\overline{P_d}/\overline{P_m}$ is illustrated in Appendix A. Bulk parameters are compared to both tidal current and free

Table 3
Principal component current error statistics at all ADCP sampling locations labeled in Fig. 1b.

Station ID	RMSE [m/s]	SI	Bias [m/s]	R
UNI001	0.117	0.373	−0.090	0.98
UNI002	0.304	0.372	−0.096	0.96
UNI003	0.541	0.534	0.270	0.97
UNI004	0.310	0.616	0.204	0.89
UNI005	0.113	0.333	−0.011	0.96
UNI006	0.591	0.496	−0.004	0.94
UNI007	0.576	0.313	0.291	0.97
UNI009	0.578	0.404	−0.220	0.97
UNI010	0.541	0.402	−0.054	0.97
UNI011	0.556	0.336	0.013	0.97
UNI012	0.422	0.500	−0.089	0.96
UNI013	0.445	1.100	0.018	0.80
UNI018	0.408	1.066	0.167	0.79
UNI019	0.606	0.625	−0.070	0.92
UNI020	0.385	0.363	−0.080	0.96
UNI021	0.395	0.919	0.206	0.85
UNI022	0.750	0.490	−0.171	0.95

Table 4
Section ID numbers (from Fig. 6) with corresponding pass place names. Dimensions for each pass are taken from Zimmermann & Prescott [15]. Form factors for free surface (F) and principal axis currents (F_U) are calculated from section averaged quantities from model output. * indicates section taken in model does not align with entire length of geographical pass.

Section ID	Pass Name	Sill Depth [m]	Length [m]	Area [m^2]	F	F_U
1	Kavalga	59	12,200	501,000	3.73	1.84
2	Tanaga*	372	33,000	4,180,000	3.21	1.17
3	Fenimore	51	6290	197,000	2.89	0.48
4	Atka	47	7640	245,000	3.55	0.48
5	Sequam	175	28,900	3,040,000	6.11	1.16
6	Samalga	246	33,400	3,750,000	1.75	0.96
7	Akutan	65	7290	195,000	3.05	0.51
8	Ugamak	88	7550	265,000	1.28	0.55

surface form factors in Fig. 10, allowing us to describe how tidal regime modulates power density. Fig. 10a reiterates that for larger current form factors, there is greater variability in monthly mean power density over the year. For semidiurnal dominated currents ($F_u < 1$), $\Delta(\overline{P_m}/\overline{P_a})$ is clustered between 0.1 and 0.2. When F_u approaches and exceeds 1 (diurnal dominated), $\Delta(\overline{P_m}/\overline{P_a})$ quickly increases to 0.4–0.6 (Fig. 10a). This confirms that seasonality to the D_1 tidal current magnitude contributes to seasonal swings in power density magnitude up to 60 % of the annual mean value, but this effect is largely unimportant for $F_u < 1$.

The spread in power density values month-to-month driven by fortnightly phase lag differences is connected to tidal regime as well, but trends differently. Sections with the largest mean range in normalized monthly power density ($\overline{\Delta \overline{P_d}/\overline{P_m}} > 3$) tend to occur at high ($F_u > 1.5$) or low ($F_u \sim 0.5$) form factors. For F_u near unity, $\overline{\Delta \overline{P_d}/\overline{P_m}}$ decreases to less than 2 (Fig. 10b), suggesting a larger spread in power density is expected month-to-month at locations with tidal current regimes approaching semidiurnal or diurnal, while locations with mixed tides feature consistent variability over the year. This effect is illustrated in Fig. 8. For any section, when the D_1 and D_2 fortnightly cycles are out of phase (as in August 2010, Fig. 8), the combined tide $\overline{P_d}$ will largely follow whatever frequency set dominates currents (section 1 for D_1, section 8 for D_2) and be biased to the appropriate fortnightly cycle. If D_1 and D_2 current magnitudes are similar (i.e., $F_u \sim 1$, section 6), neither fortnightly cycle dominates the combined tide, and P_d instead holds a moderate, less varied value for an extended period as the equal magnitude tide groups pulse in succession.

The correlation coefficient between φ and $\Delta \overline{P_d}/\overline{P_m}$ emphasizes that mixed tides are more sensitive to fortnightly phase lags. $\rho_{\Delta \overline{P_d},\varphi}$ shows a maximized linear trend exactly at $F_u = 1$ ($\rho_{\Delta \overline{P_d},\varphi} = -0.8$) which reduces sharply ($\rho_{\Delta \overline{P_d},\varphi} = -0.2$ to 0.2) as F_u deviates from unity (Fig. 10c). Sections with nearly equal D_1 and D_2 current magnitudes therefore tend to feature reduced ranges in monthly power densities for higher phase lag times (as explained in the preceding paragraph for an out of phase scenario), and enhanced ranges in power density for small φ, presumably from D_1 and D_2 cycles interacting constructively. At less "mixed" sections where D_1 or D_2 tides dominate, the φ correlation is weak, as one tide group always is large enough to exert control, regardless of destructive or constructive fortnightly phasing (e.g., Fig. 8j–l).

Lastly, we note another important result of Fig. 10: the lack of trend between free surface form factor and power density parameters (Fig. 10d, e, f). Tidal regime defined by currents illustrate $F_u = 1$ to be a generally clear and important threshold dictating power density variability over the year in the Aleutians. Yet, the conventional form factor, F, which is perhaps more widely applied in defining tidal regime for oceanographic purposes, appears largely useless for tidal stream power estimates. Indeed, it is well understood that tidal current and free surface amplitudes will not (and often do not) scale, but we highlight that dichotomy here as an important consideration when characterizing tidal regimes for tidal stream power purposes. When it comes down to it, currents must be measured to estimate power generation variability from currents.

5. Discussion

5.1. Implications of Tidal Regime on Energy Resource

The results of this work reveal a few, notable implications for the future scientist or engineer to consider when performing tidal energy resource assessments. This study makes it clear that the time periods we take temporal mean quantities over is consequential to tidal stream resource parameters such as the mean kinetic energy flux, *KEF*, and annual available energy, *AAE*. This is particularly true in regions with mixed tides. Often, 15 or 30 days are used and considered representative of conditions as a spring-neap cycle is captured (e.g., Ref. [22–24]). This work illustrates that may be a poor strategy in regions where $F_u > 1$, and values such as $\overline{P_m}$ can be ± 40 % of the annual mean depending on season (Fig. 9). Should a poorly representative mean P be applied to annual energy estimates (*KEF* or *AAE*), then the tidal energy potential of a region could be grossly misrepresented. Globally, there are many regions of strong, mixed tides where this could be relevant: Eastern Russia, Alaska, the West Coast of the United States, Southeast Asia, Australia, amongst others.

This work also highlights the importance of using tidal current measurements to parameterize the impact of tidal regime on tidal stream energy resources. Although imperfect, there is a more definitive relationship to power metrics for form factors derived from currents (F_u) compared to those from free surface elevations (F) (Fig. 10). In the Aleutians, and likely elsewhere, regional tidal propagation and local topography create tidal current regimes which do not always align with what would be expected from surface elevation (i.e., tide gauge) measurements alone. So, although a coastal practitioner may estimate the impact of tidal regime on annual variation in power density at a given location, they would require an estimate of F_u to confidently do so, not F. An immediately applicable result of this work is the ability to infer tidal stream power density variability over a year based on any, shorter (i.e., not full year) time series of current velocity which allows for reasonable estimates of F_u.

Lastly, we have shown that some passes in the Aleutian Islands experience significant seasonal modulation to tidal currents and power density, while others do not (Fig. 9). Those with $F_u > 1$ will see significant swings in monthly averaged power density, while those with $F_u \sim 1$ will experience more inconsistent ranges in power density month-to-month. This information can be powerful when leveraged during tidal

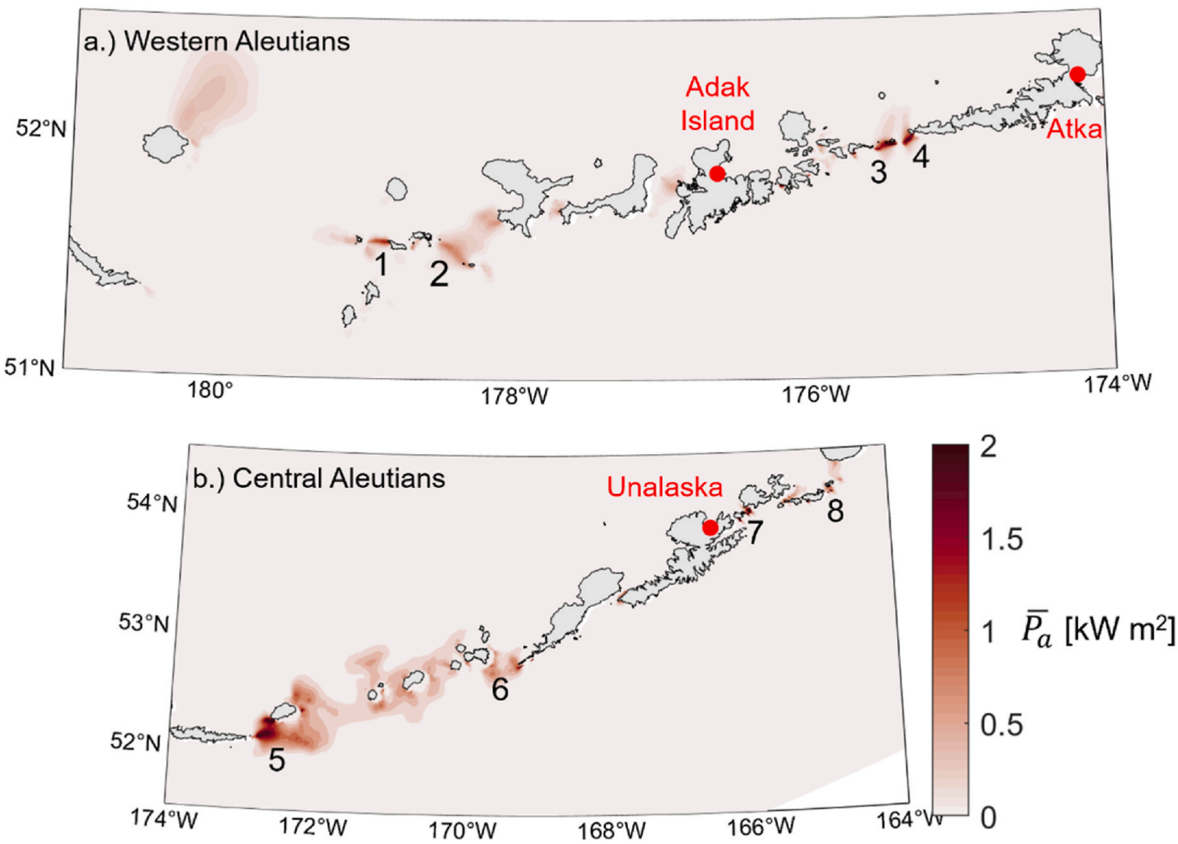

Fig. 6. Colored contours of 365-day mean, depth-averaged power densities, $\overline{P_a}$, over the western (a) and central (b) Aleutian Islands. Eight "hotspots" are labeled, with 1 thru 4 in (a) and 5 thru 8 in (b) which correspond to the passes described in Table 4. Three NOAA tide gauge locations are labeled with red dots as location references. (For interpretation of the references to color in this figure legend, the reader is referred to the Web version of this article.)

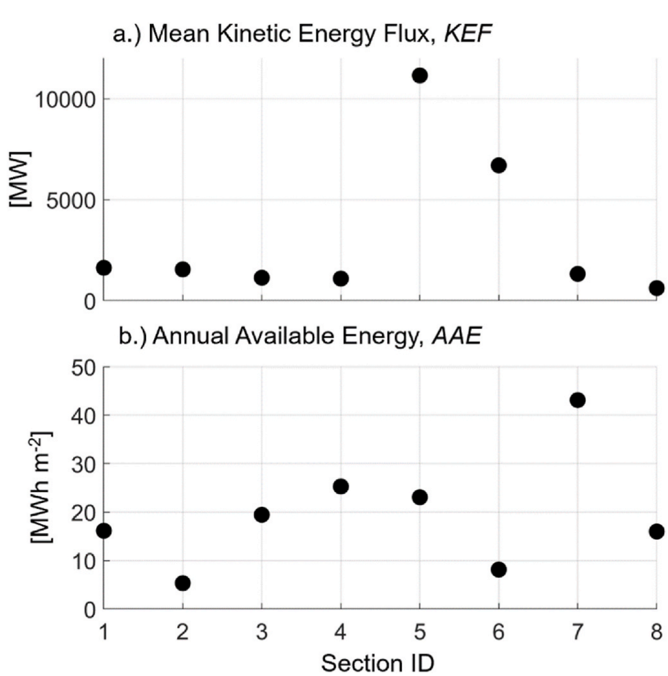

Fig. 7. 365-day averages of kinetic energy flux (a) and annual available energy (b) at each section (x-axis) labeled in Fig. 6.

turbine siting. Depending on local needs, it may be important to sustain a near-constant stream of tidal energy throughout the year, which would make sections 3, 4, 7, and 8 most favorable (Fenimore, Atka, Akutan, and Ugamak Passes). Sections 1, 2, 5, and 6 will experience seasonal change to mean power (Kavalga, Tanaga, Sequam, and Samalga Passes). If municipalities near these "seasonal" passes can be easily powered during periods of tidal stream energy minima (i.e., autumn and spring), there is also opportunity to sell excess energy during periods of higher energy (summer, winter) elsewhere. Further, it could be that excess power produced in the autumn months can be stored locally to augment power in winter, when daylight is shorter, temperatures are colder, and power demand is generally maximized. Similarly, sections 2, 5, and 6 will have seasonal variation to monthly power ranges, while sections 1, 3, 4, 7, and 8 will largely not. The consistency of monthly tidal stream power ranges could also be impactful to community needs and should be considered prior to development.

5.2. Limitations

The impact of tidal regime on tidal stream power density in eight Aleutian Island passes has been quantified. Seasonal modulation to D_1 current magnitudes and offset fortnightly D_1 and D_2 tidal cycles modulate monthly mean and range in power density: with both showing a dependence to current form factor, F_u. Even so, results do not show perfect consistency across all sections, as some locations deviate from the broader trend (e.g., Fig. 10a, b, c), warranting further discussion.

Sustained tidal asymmetry in currents exists at several locations in the Aleutians (e.g., Section 1, Fig. 8a) due to strong interaction amongst the K_1, O_1, and M_2 frequencies and likely significant bathymetric and geometric-created nonlinearities [34]. Asymmetry varies in importance over the D_1 spring-neap cycle and can be modified by the phase alignment between D_1 and D_2 tides. Even so, it is not clear if tidal asymmetry in currents could allow monthly scale modulation to power density.

Related to the former point: the analysis employed in this work fo-

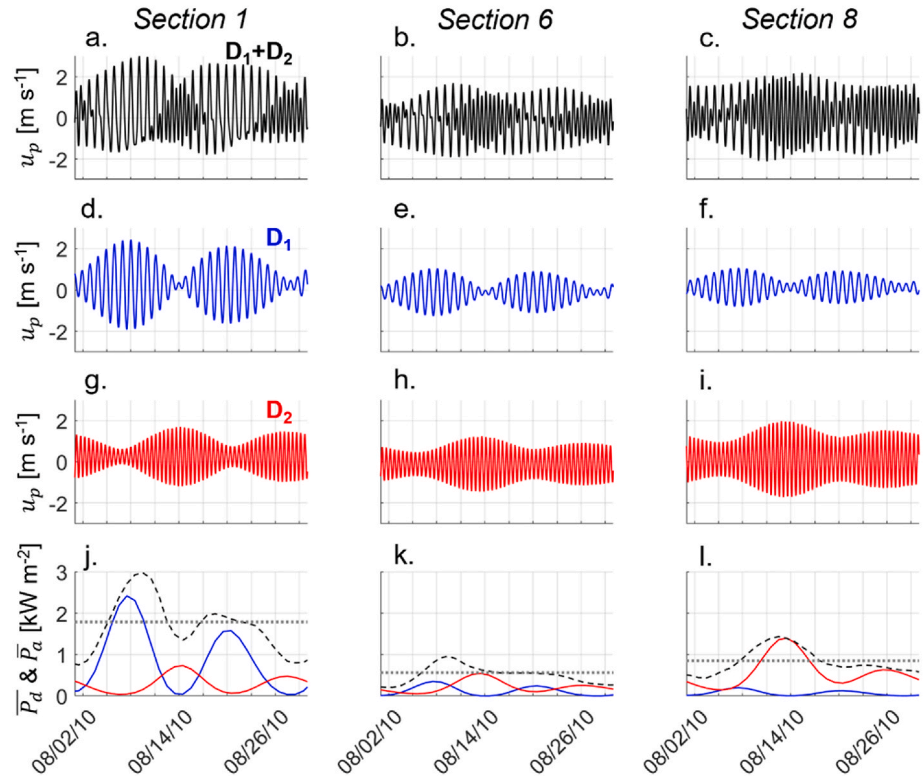

Fig. 8. Times series of reconstructed section-averaged principal current velocity, u_p, using all eight astronomical tidal harmonics forcing the model (black: a, b, c), the four diurnal constituents only (blue: d, e, f), and the four semidiurnal constituents only (red: g, h, i) at sections 1 (left panels), 5 (middle panels), and 8 (right panels) for August 2010. Daily (25 h) mean power densities associated with each group of frequencies (in same colors) are given in bottom panels (j, k, l) with annual mean (dotted gray). (For interpretation of the references to color in this figure legend, the reader is referred to the Web version of this article.)

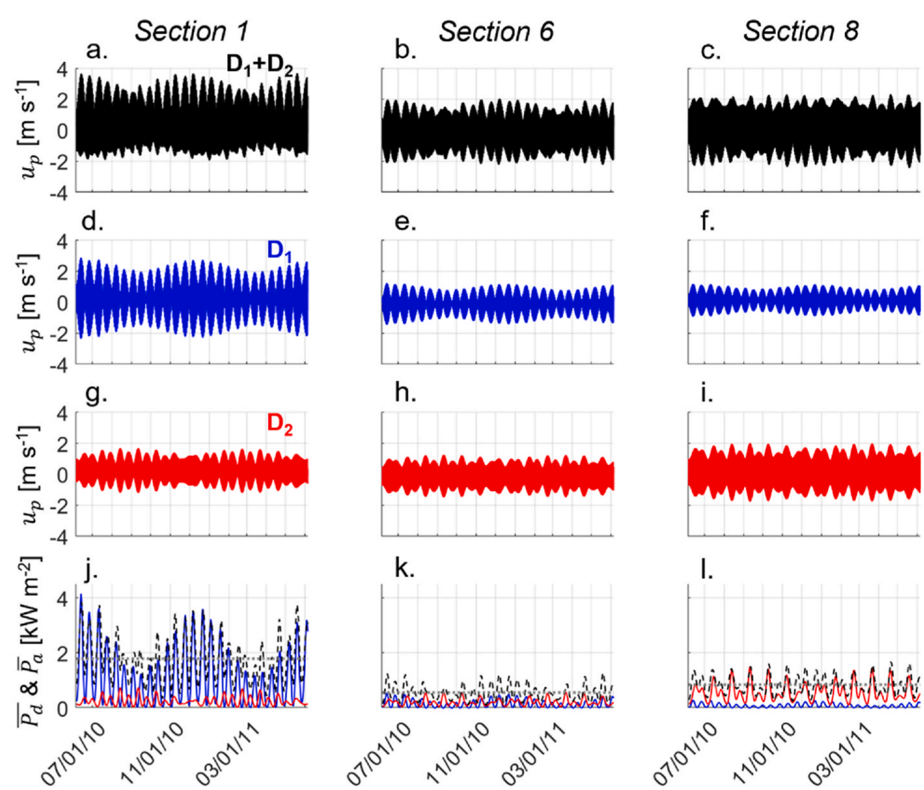

Fig. 9. Same as Fig. 8 but for the year-long period of June 5, 2010, to June 5, 2011. Note: y-axes are on larger scales than Fig. 8.

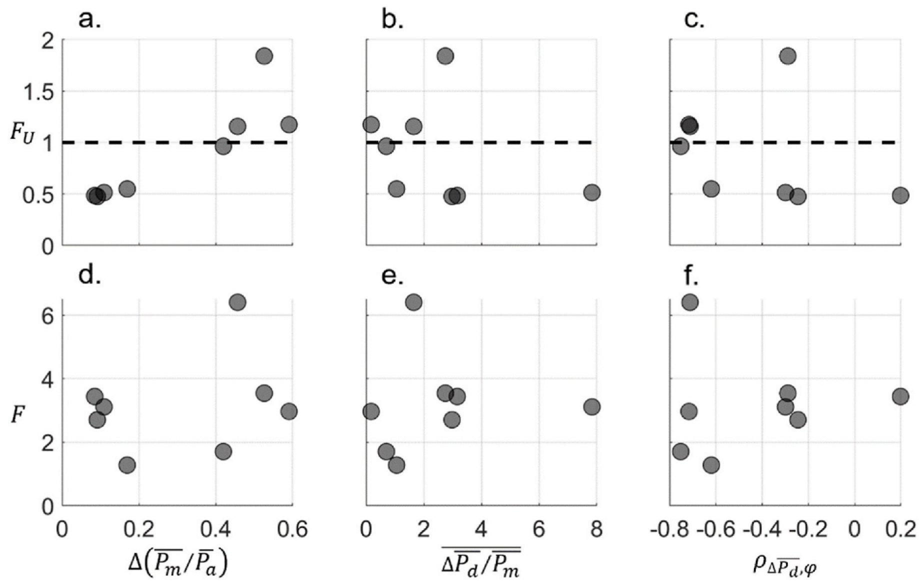

Fig. 10. (a, d) Annual range in normalized monthly mean power density, $\Delta(\overline{P_m}/\overline{P_a})$, (b, e) annual mean in normalized daily mean power density range, $\overline{\Delta \overline{P_d}/\overline{P_m}}$, and (c, f) correlation coefficient between normalized daily mean power density and fortnightly phase lag, $\rho_{\Delta \overline{P_d},\varphi}$ (x-axes) for each section classified by (a, b, c) tidal current form factor, F_U, and (d, e, f) free surface form factor, F. $F_U = 1$ is marked with a dashed black line in (a, b, c).

cuses on four constituents in the D_1 frequency band and four in the D_2. It is likely that higher frequency overtides and compound tides are influential at some locations but are not captured in the decomposition we utilize. Depending on the magnitude and spatial extent of the neglected frequencies, they could play a role in power density parameters not captured in our simplified F_u and F comparison (Fig. 10). The nondimensional numbers could possibly be re-worked to include the influence of nonlinear effects in the future and would be a worthy next step to pursue in this line of work.

Unrelated to analysis techniques, the numerical model we utilize carries some limitations worth mentioning. The wave environment around the Aleutians is one of the most energetic, globally [28], and wave-current interaction could be consequential to tidal energy potential. We omitted the influence of waves from these simulations to focus strictly on tides, but future work would do well to consider their impact. Further, our model is run in barotropic mode and discounts baroclinic processes. It has been shown that large amplitude internal waves occur around the Aleutians that can create significant currents [35,36], and internal tides occur which dissipate M_2 barotropic tidal energy [13]. These waves are not included in our model, and therefore add a degree of uncertainty to our simulations. Lastly, this modeling work focuses on the unaltered (no turbine) power density of depth averaged currents around the Aleutians. The physically extractable tidal stream power likely scales with P, but there could be differences depending on turbine type, array size, and configuration. Investigating the effect of mixed tides on physically extractable power scenarios is an important future research path.

6. Conclusions

This study characterized and quantified the undisturbed tidal stream energy resource of eight major passes in the Aleutian Islands region of Alaska using a year-long simulation of a validated tidal hydrodynamic model. The annual mean kinetic energy flux, *KEF*, was calculated and found to vary between ~1000 MW (Ugamak Pass) and ~11,000 MW (Sequam Pass) over the region. The geometry-independent annual available energy, *AAE*, was identified to be largest in Akutan Pass (42 MWh m^{-2}) and smallest in Tanaga Pass (5 MWh m^{-2}).

Significant spatial variability in the seasonal modulation of power densities was identified, quantified, and linked to tidal regime. We found that passes with tidal current form factors, F_u, greater than unity (i.e., diurnal currents dominate) experience the strongest seasonal variability in power density. Monthly mean P at those locations increase (decrease) by 20–40 % relative to the annual mean in winter/summer (spring/autumn), with the magnitude of variability scaling with F_u. Semi-annual adjustment occurs primarily due to seasonal modulation of the D_1 tidal amplitude, created by changes to solar declination over the year, but also from varying constructive/destructive interference of D_1 and D_2 fortnightly cycles which fall in/out of phase over a similar ~177-day period. We find that the offset fortnightly cycles are connected to monthly ranges in power density. Passes with $F_u \sim 1$ generally have the smallest normalized ranges in power density ($\overline{\Delta \overline{P_d}/\overline{P_m}} < 2$), as neither the D_1 nor D_2 frequencies exert dominance over the other. We corroborate this by showing passes with $F_u \sim 1$ have the strongest correlation between fortnightly phase lag and power density range ($\rho_{\Delta \overline{P_d},\varphi} \sim -0.8$): when phase lags are largest, monthly power density ranges are smallest. The opposite trends were found when F_u diverges from unity: average normalized ranges in power density increase when one tidal frequency band becomes dominant, and the correlation between phase lag and range becomes progressively weaker as either the D_1 or D_2 tide increases in amplitude.

Seasonal modulation to tidal stream energy resources is clearly important to consider in the Aleutian Islands, and likely in other regions with mixed tides. Importantly, we find that tidal regimes determined by currents, not water levels, predict annual variability in power density. This topic has received little attention in former studies. Future work would do well to test the general applicability of these results in other regions and augment this analysis with consideration of nonlinear tides. The authors hope this study will serve as a framework to inspire further investigation of the topic.

CRediT authorship contribution statement

Preston Spicer: Writing – review & editing, Writing – original draft, Visualization, Validation, Software, Resources, Methodology, Investigation, Formal analysis, Data curation, Conceptualization. **Zhaoqing Yang:** Writing – review & editing, Supervision, Resources, Project administration, Methodology, Funding acquisition, Conceptualization. **Taiping Wang:** Writing – review & editing, Validation, Software, Resources, Methodology, Investigation. **Mithun Deb:** Writing – review & editing, Validation, Resources, Methodology, Investigation.

Declaration of competing interest

The authors declare the following financial interests/personal relationships which may be considered as potential competing interests: Preston Spicer, Zhaoqing Yang, Taiping Wang, Mithun Deb reports financial support was provided by US Department of Energy. Zhaoqing Yang reports a relationship with International Journal of Renewable Energy Research that includes: board membership. If there are other authors, they declare that they have no known competing financial interests or personal relationships that could have appeared to influence the work reported in this paper.

Acknowledgments

This study was funded by the U.S. Department of Energy, Office of Energy Efficiency and Renewable Energy, Water Power Technologies Office under contract DE-AC05-76RL01830 at the Pacific Northwest National Laboratory (PNNL). Model simulations were performed using PNNL's Institutional Computing facility as well as the Eagle and Kestrel high-performance computing systems at the National Renewable Energy Laboratory (NREL). The authors thanks two anonymous reviewers for their help improving the manuscript.

Appendix A

Figure A.1 illustrates the quality of reconstructed principal axis tidal current time series when applying eight major astronomical constituents: M_2, S_2, K_2, N_2, K_1, O_1, P_1, and Q_1. The residual, taken as the difference between the modeled tidal current and the reconstructed, may be considered the portion of the modeled current found in tidal constituents other than those listed above. Here, we see the residual amplitude maximizes at ~0.8 m/s at section 1, though is often less. At sections 6 and 8, the residual never exceeds 0.4 m/s (Fig. A.1). At all sections, the vast majority of the modeled current signal is captured in the full-year reconstructed time series, evident in percent tidal variance values ranging from 96.2 % (section 1) to 99.0 % (section 7), suggesting inclusion of other, less significant constituents is not necessary for accurate reconstruction.

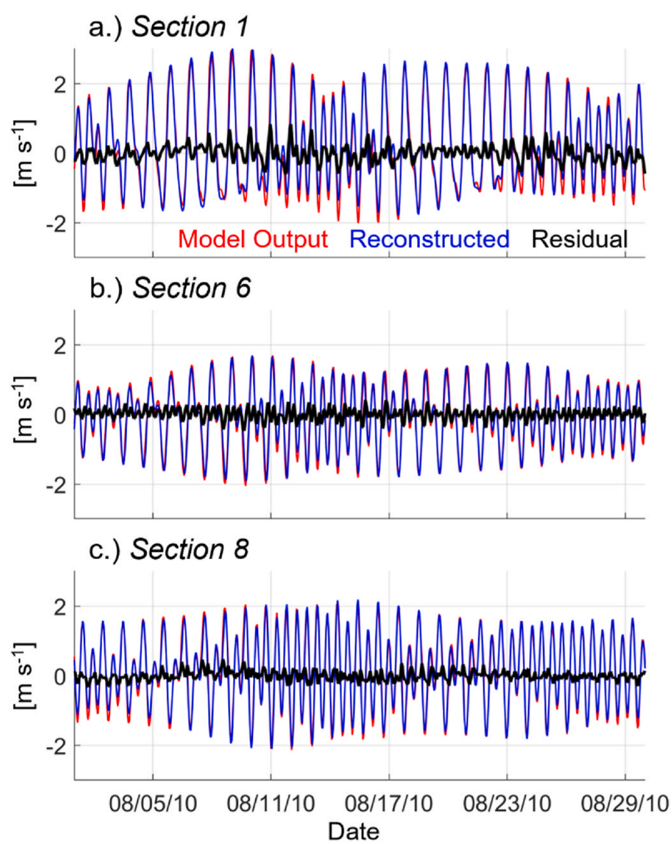

Fig. A.1. Times series of model-produced (red) and the 8 astronomical constituent reconstructed (blue) section-averaged principal current velocities, u_p, at sections 1 (a), 6 (b), and 8 (c). The difference between model and reconstructed time series is the residual, given in black.

Appendix B

As inferred from Fig. 9, seasonal variation to P occurs with significant dependence on location and relative strength of diurnal currents (Fig. B.1a). At sections 1, 2, 5, and 6, $\overline{P_m}$ is reduced around the autumnal (August thru October) and vernal equinox (February thru April): typically minimizing between 60 % and 80 % of $\overline{P_a}$. At the same sections, the largest $\overline{P_m}$ occurs around the summer (May thru July) and winter (November thru January) solstices at 120 %–140 % of $\overline{P_a}$ (Fig. B.1a). At sections 3, 4, 7, and 8, monthly variability is strikingly muted compared with the other sections. Marginal increases (decreases) in $\overline{P_m}$ still occur in the winter/summer (spring/fall) but generally at ± 5 % of the annual mean (Fig. B.1a). The sections with the largest swings in seasonal currents, and therefore power density (1, 2, 5, and 6), feature the largest diurnal contributions to currents with $F_U \geq \sim 1$

(Table 4).

Variability to $\overline{P_d}$ within each month is not as obviously connected to tidal regime and shows more extreme spatial change relative to temporal (Fig. B.1b). The largest monthly spread in power density relative to monthly mean occurs at section 7 where $\Delta\overline{P_d}$ is 7–8 times larger than $\overline{P_m}$. Sections 1, 3, 4, and 5 are similar with $\Delta\overline{P_d}/\overline{P_m}$ between 3 and 6, and sections 2, 6, and 8 show the smallest monthly ranges with $\Delta\overline{P_d}/\overline{P_m}$ typically less than 2 (Fig. B.1b). It appears the larger time-averaged $\Delta\overline{P_d}/\overline{P_m}$ occur at sections with low F_U (~0.5 or sections 3, 4, 7) or high F_U (1.84 or section 1). The remaining sections are characterized by intermediate F_U values (0.55–1.17) and feature relatively reduced $\Delta\overline{P_d}/\overline{P_m}$ (sections 2, 5, 6, 8).

Temporal variation to $\Delta\overline{P_d}/\overline{P_m}$ is more nuanced. Seasonal change to the normalized monthly power density range appears to occur at most sections (apart from 3 to 4) with varying influence. As the seasonal modulation to D_1 mean power is omitted in Fig. B.1b, we can assume that seasonal variability to $\Delta\overline{P_d}$ here is a result of the D_1 and D_2 fortnightly phase lag, mentioned previously. The 5–20 % reductions in $\Delta\overline{P_d}$ relative to $\overline{P_m}$ occurring in August thru October and February thru March at most sections (Fig. B.1b) align with periods of maximal phase difference in fortnight periods (~6 days, illustrated in Fig. 7). Over the remainder of the year, the fortnightly cycles drift closer together and lag only by their difference in period near December and June (~1.1 days, not shown), when $\Delta\overline{P_d}/\overline{P_m}$ is largest at each section. These results suggest the D_1 to D_2 fortnightly phase lag is important to seasonal modulation of power density at some sections, by either enhancing or damping power density ranges over each month. Unlike the seasonal adjustment due to D_1 magnitude (Fig. B.1a), it is not as clear which tidal regime is most affected. Sections with the greatest $\Delta\overline{P_d}/\overline{P_m}$ temporal variability do not necessarily align with spatially highest or lowest $\Delta\overline{P_d}/\overline{P_m}$.

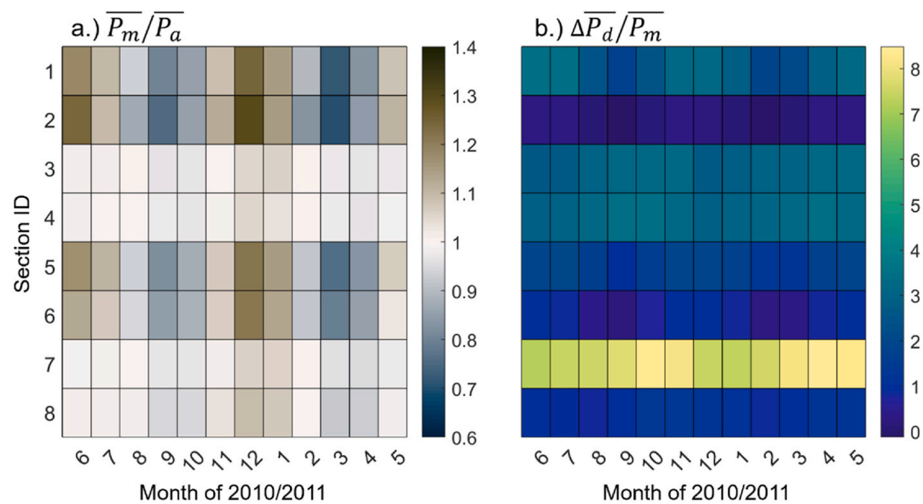

Fig. B.1. (a) Hovmoller panel plot of monthly mean power density, $\overline{P_m}$ (colorbar) normalized by annual mean, $\overline{P_a}$, for each month (*x*-axis) at each section (*y*-axis). (b) Same, but for range in daily mean power density, $\Delta\overline{P_d}$, relative to $\overline{P_m}$.

References

[1] K.A. Haas, H.M. Fritz, S.P. French, B.T. Smith, V.S. Neary, Assessment of energy production potential from tidal streams in the United States. https://www.osti.gov/biblio/1219367, 2011.
[2] L. Kilcher, M. Fogarty, M. Lawson, Marine energy in the United States: An overview of opportunities (2021).
[3] G. Holdmann, D. Pride, G. Poelzer, B. Noble, C. Walker, Critical pathways to renewable energy transitions in remote Alaska communities: a comparative analysis, Energy Res. Social Sci. 91 (2022) 102712, https://doi.org/10.1016/j.erss.2022.102712.
[4] EIA, Alaska State Energy Profile, U.S. Energy Information Administration, 2023. Retrieved March 15 from, https://www.eia.gov/state/print.php?sid=AK.
[5] J.B. Johnson, D.J. Pride, River, tidal, and ocean current hydrokinetic energy technologies: status and future opportunities in Alaska, Prepared for Alaska Center for Energy and Power (2010).
[6] S. Kist, S. Hinman, ORPC Partnering with Matanuska-Susitna Borough to Trial RivGen® Power System in Upper Cook Inlet (2022, April 5).
[7] T. Wang, Z. Yang, A tidal hydrodynamic model for Cook Inlet, Alaska, to support tidal energy resource characterization, J. Mar. Sci. Eng. 8 (4) (2020) 254.
[8] M. Foreman, P. Cummins, J. Cherniawsky, P. Stabeno, Tidal energy in the Bering Sea, J. Mar. Res. 64 (6) (2006) 797–818.
[9] P.J. Stabeno, D.G. Kachel, N.B. Kachel, M.E. Sullivan, Observations from moorings in the Aleutian Passes: temperature, salinity and transport, Fish. Oceanogr. 14 (s1) (2005) 39–54, https://doi.org/10.1111/j.1365-2419.2005.00362.x.
[10] C. Fredenberg, Wind energy development in the aleutian Pribilof Islands, Aleutian Pribilof Islands Association (2006).
[11] Y. Li, L. Willman, Feasibility analysis of offshore renewables penetrating local energy systems in remote Oceanic areas – a case study of emissions from an electricity system with tidal power in Southern Alaska, Appl. Energy 117 (2014) 42–53, https://doi.org/10.1016/j.apenergy.2013.09.032.
[12] B.A. Wright, Feasibility of Tidal and Ocean Current Energy in False Pass, Aleutian Islands (2014). *Alaska final report*.
[13] B.R. Joyce, W.J. Pringle, D. Wirasaet, J.J. Westerink, A.J. Van der Westhuysen, R. Grumbine, J. Feyen, High resolution modeling of western Alaskan tides and storm surge under varying sea ice conditions, Ocean Model. 141 (2019) 101421, https://doi.org/10.1016/j.ocemod.2019.101421.
[14] W. Guo, D. Song, X.H. Wang, P. Ding, J. Ge, Contributions of different tidal interactions to fortnightly variation in tidal duration asymmetry, J. Geophys. Res.: Oceans 121 (8) (2016) 5980–5994, https://doi.org/10.1002/2016JC011689.
[15] M. Zimmermann, M.M. Prescott, Passes of the Aleutian Islands: first detailed description, Fish. Oceanogr. 30 (3) (2021) 280–299, https://doi.org/10.1111/fog.12519.
[16] Z. Kowalik, Bering Sea tides, in: T.R. Loughlin (Ed.), Dynamics of the Bering Sea: a Summary of Physical, Chemical, and Biological Characteristics, and a Synopsis of Research on the Bering Sea, University of Alaska Sea Grant, 1999, pp. 93–127.
[17] R. Reed, P. Stabeno, Flow along and across the Aleutian ridge, J. Mar. Res. 52 (4) (1994) 639–648.
[18] R. Reed, P. Stabeno, Long-term measurements of flow near the Aleutian Islands, J. Mar. Res. 55 (3) (1997) 565–575.
[19] C. Garrett, Tidal resonance in the Bay of Fundy and Gulf of Maine, Nature 238 (5365) (1972) 441–443, https://doi.org/10.1038/238441a0.
[20] C. Chen, H. Liu, R.C. Beardsley, An unstructured grid, finite-volume, three-dimensional, primitive equations ocean model: application to coastal ocean and estuaries, J. Atmos. Ocean. Technol. 20 (1) (2003) 159–186, https://doi.org/10.1175/1520-0426(2003)020<0159:AUGFVT>2.0.CO;2 [Article].
[21] IEC, in: Technical Specification: Marine Energy - Wave, Tidal and Other Water Current Converters - Part 201: Tidal Energy Resource Assessment and Characterization, IEC TS vols. 62600–201, 2015, p. 44.
[22] M. Deb, Z. Yang, T. Wang, L. Kilcher, Turbulence modeling to aid tidal energy resource characterization in the Western Passage, Maine, USA, Renew. Energy 219 (2023) 118694, https://doi.org/10.1016/j.renene.2023.04.100.
[23] P. Spicer, P. MacCready, Z. Yang, Localized tidal energy extraction in puget sound can adjust Estuary reflection and friction, modifying barotropic tides system-wide, J. Geophys. Res.: Oceans 129 (5) (2024) e2023JC020401, https://doi.org/10.1029/2023JC020401.
[24] P. Spicer, Z. Yang, T. Wang, M. Deb, Tidal energy extraction modifies tidal asymmetry and transport in a shallow, well-mixed Estuary, Front. Mar. Sci. 10 (2023) 1268348.

[25] Z. Yang, T. Wang, R. Branch, Z. Xiao, M. Deb, Tidal stream energy resource characterization in the Salish Sea, Renew. Energy 172 (2021) 188–208.
[26] M. Zimmermann, M.M. Prescott, C.N. Rooper, Smooth sheet bathymetry of the Aleutian Islands. https://repository.library.noaa.gov/view/noaa/4426, 2013.
[27] T. Ezer, L.-Y. Oey, On the dynamics of strait flows: an ocean model study of the Aleutian passages and the Bering Strait, Ocean Dyn. 63 (2) (2013) 243–263, https://doi.org/10.1007/s10236-012-0589-6.
[28] G. García-Medina, Z. Yang, W.-C. Wu, T. Wang, Wave resource characterization at regional and nearshore scales for the U.S. Alaska Coast based on a 32-year high-resolution hindcast, Renew. Energy 170 (2021) 595–612, https://doi.org/10.1016/j.renene.2021.02.005.
[29] G.D. Egbert, S.Y. Erofeeva, Efficient inverse modeling of Barotropic Ocean tides, J. Atmos. Ocean. Technol. 19 (2) (2002) 183–204, https://doi.org/10.1175/1520-0426(2002)019<0183:Eimobo>2.0.Co;2.
[30] G. Deng, Z. Zhang, Y. Li, H. Liu, W. Xu, Y. Pan, Prospective of development of large-scale tidal current turbine array: an example numerical investigation of Zhejiang, China, Appl. Energy 264 (2020) 114621.
[31] Z. Yang, T. Wang, A. Copping, S. Geerlofs, Modeling of in-stream tidal energy development and its potential effects in Tacoma Narrows, Washington, USA, Ocean Coast Manag. 99 (2014) 52–62, https://doi.org/10.1016/j.ocecoaman.2014.02.010.
[32] S. Ahn, K.A. Haas, V.S. Neary, Wave energy resource characterization and assessment for coastal waters of the United States, Appl. Energy 267 (2020) 114922.
[33] D.L. Codiga, Unified tidal analysis and prediction using the UTide matlab functions. ftp://www.po.gso.uri.edu/pub/downloads/codiga/pubs/2011Codiga-UTide-Report.pdf, 2011.
[34] N.J. Nidzieko, Tidal asymmetry in estuaries with mixed semidiurnal/diurnal tides, J. Geophys. Res.: Oceans 115 (C8) (2010).
[35] P.F. Cummins, J.Y. Cherniawsky, M.G. Foreman, North Pacific internal tides from the Aleutian Ridge: altimeter observations and modeling, J. Mar. Res. 59 (2) (2001) 167–191.
[36] Z. Kowalik, Tide distribution and tapping into tidal energy, Oceanologia 46 (3) (2004).